Materials Today Energy 29 (2022) 101112

Contents lists available at ScienceDirect

Materials Today Energy

journal homepage: www.journals.elsevier.com/materials-today-energy/

Highly dispersed face-centered cubic copper–cobalt alloys constructed by ultrafast carbothermal shock for efficient electrocatalytic nitrate-to-ammonia conversion

Ye Chen [a], Yaling Zhao [b], Ziwei Zhao [a], Yang Liu [a, *]

[a] School of Materials Science and Engineering, Henan Normal University, Xinxiang, Henan 453007, PR China
[b] School of Chemistry and Chemical Engineering, Henan Normal University, Xinxiang, Henan 453007, PR China

ARTICLE INFO

Article history:
Received 23 June 2022
Received in revised form
30 July 2022
Accepted 1 August 2022
Available online 5 August 2022

Keywords:
Nitrate reduction to ammonia
Ammonia synthesis
Bimetallic alloy
Carbothermal shock

ABSTRACT

Ammonia is a promising new generation of green energy that has the potential to replace hydrogen energy and facilitate the energy structure optimization of human society. However, the technology of green ammonia production under ambient conditions is still immature. It is urgent to develop new strategies for efficient and green ammonia production adapted to distributed energy, resource environment, and human health. Hereon, a highly dispersed face-centered cubic copper–cobalt alloy was prepared by ultrafast carbothermal shock for green ammonia production from nitrate under ambient conditions. The $Cu_{2.5}Co$ alloy achieves a remarkable ammonia yield of 164.23 μmol/h/cm^2 and an exceptional faradaic efficiency of 96.29% at −0.25 V and −0.05 V versus reversible hydrogen electrode in a neutral solution. The electronic regulation of Co on Cu reduces the Tafel slope from 182 mV/dec of monometallic Cu to 108 mV/dec of bimetal $Cu_{2.5}Co$ alloy; the addition of Co optimizes the overall catalytic activity of the catalyst. This work provides a new idea for the design and synthesis of high-efficiency electrocatalyst for green ammonia production from nitrate and water under ambient conditions.

1. Introduction

Nitrate (NO_3^-) and ammonia (NH_3) are essential components of the global nitrogen cycle [1]. Over a century ago, Haber and Bosch et al. made persistent efforts to artificially prepare active nitrogen that could be absorbed and used by crops, pioneering the conversion of nitrogen (N_2) from air to NH_3, which is crucial for increasing global food production, population size, and sustainable economic and social development [2,3]. The Haber-Bosch process is the dominant method of ammonia synthesis in the industry nowadays, which features harsh reaction conditions, energy-intensive, and is not easy to stop at any time [4,5]. In addition, the content of NO_3^- in groundwater and surface water is increasing with the application of large amounts of agricultural fertilizers every year, and the hard-to-treat NO_3^- poses a significant threat to human life and health [6]. In the context of the energy crisis and carbon neutrality, it is encouraging and exciting to explore new and complementary pathways of NH_3 production from the global nitrogen cycle that can serve as an integrated solution for energy, environment, and human health [7].

Electrocatalytic NO_3^- reduction to NH_3 (NRA) offers an attractive strategy to address NO_3^- contamination and can achieve high-efficiency NH_3 production under ambient conditions [8,9]. The enormous NO_3^- arising from fertilizer loss is more easily converted to NH_3 than N_2 in reaction kinetics, which is receiving more and more attention. Cu has been widely studied for its excellent NRA activity [10–12], where the Cu(111) plane is highly active at low overpotentials, while the Cu(100) plane is highly active at high overpotentials [13,14]. The adsorption and reduction of NO_3^- is enhanced on Cu(111) because the Cu(111) with a similar crystal surface of Cu_2O is more easily oxidized [15]. Wang et al. reported CuO nanowire arrays for electrocatalytic NO_3^- reduction to NH_3, Cu/Cu_2O converted from CuO serves as the dominant active site [16]. Sargent's group demonstrated a $Cu_{50}Ni_{50}$ alloy that achieved a remarkable Faradaic efficiency of ~99% [17]. The additive Ni atoms raise the d-band center of the Cu atoms, which enhances the adsorption energy for NO_3^- and reduces the reaction energy barrier of the rate-determining step. Li et al. synthesized a unique Ru/

* Corresponding author.
E-mail address: liuyang20208@htu.edu.cn (Y. Liu).

https://doi.org/10.1016/j.mtener.2022.101112
2468-6069/

oxygen-doped-Ru core/shell nanoclusters, the tensile strain on the Ru surface raises the reaction energy barrier for the coupling of double H atoms, which facilitates the generation of hydrogen radicals and substantially increases the rate of ammonia production [18].

Inspired by the mechanisms mentioned above of heteroatoms and lattice stress on the d-band centers of Cu atoms, we investigated the regulation of Co content on the catalytic activity of copper−cobalt alloys synthesized by carbothermal shock. The Co tends to form a face-centered cubic structure below 20 nm and at high temperatures, similar to Cu's lattice. The Co atoms with three d-orbital single electrons have a higher d-band center than Ni atoms and are more advantageous in tuning the electronic structure of Cu. The $Cu_{2.5}Co$ alloy achieves a high ammonia yield of 164.23 μmol/h/cm^2 and an outstanding faradaic efficiency of 96.29% at −0.25 V and −0.05 V versus reversible hydrogen electrode (vs. RHE) in a neutral solution, the electron-modulating effect of Co on Cu atoms optimizes the rate-determining step and increases the total reaction active.

2. Experimental section

2.1. Chemicals and materials

All the reagents were of analytical grade and used directly without further purification. The ammonium chloride (NH_4Cl), nitrate of potash ($^{14}KNO_3$), nitrate of potash ($^{15}KNO_3$), and sodium nitrite ($NaNO_2$) were purchased from Sigma-Aldrich. The nickel chloride hexahydrate ($NiCl_2{\cdot}6H_2O$), cobalt chloride hexahydrate sodium ($CoCl_2{\cdot}6H_2O$), sodium hypochlorite (NaClO), sodium hydroxide (NaOH), sodium salicylate ($C_7H_5NaO_3$), and sodium nitroferricyanide (III) dihydrate (Na_2 [$Fe(CN)_5NO$]$\cdot 2H_2O$) were provided by Shanghai Aladdin Biochemical Technology Co., Ltd. The carbon fiber paper (CFP) with a thickness of 2 mm was obtained from Suzhou Sunernuo Technology Co., LTD. All solutions involved during the experiment were prepared using deionized water with a resistivity of 18.25 MΩ.

2.2. Preparation of the copper−cobalt alloys

The hydrophilicity of CFP (1.0 × 0.5 cm^2) was enhanced by a calcining process with an alcohol lamp for 60 s, the calcined CFP was dipped into a mixed metal salt solutions of $NiCl_2{\cdot}6H_2O$ and $CoCl_2{\cdot}6H_2O$ (0.1 mol/L for the total metal elements) and dried under the electric baking lamp (180 W) for 3 min until completely dry.

The carbothermal shock process was carried out by electrically-triggered Joule heating of precursor-loaded CFP films in a 95 vol% Ar-5 vol% H_2 atmosphere [19,20]. The sample mentioned above was suspended on a quartz plate by connecting CFP to two copper electrodes, which was driven and controlled by an external power source (Keithley 2425 SourceMeter), a 60 ms electrical pulse was chosen as the thermal shock duration for the synthesis of copper−cobalt alloy in this work. After the energization, a 1-min cooling process was performed in a 95 vol% Ar-5 vol% H_2 atmosphere to avoid oxidation of the sample. A series of samples with the Cu:Ni ratios of 1:0, 5:1, 2.5:1, 1:1 and 0:1 were prepared and were named Cu-CFP, Cu_5Co-CFP, $Cu_{2.5}Co$-CFP, CuCo-CFP, and Co-CFP.

2.3. Catalyst characterization

The morphology and size distribution of copper−cobalt alloy were characterized by using a field-emission scanning electron microscope (FE-SEM, Zeiss Supra 40, Japan) and transmission electron microscope (TEM, JEOL JEM-2100, Japan). The information of crystal texture and phonon vibration were analyzed by X-ray diffraction instrument (XRD, Bruker D8 advance Diffractometer, Bruker Germany) and Raman micro-spectrometer (LabRAM HR Evolution, Horiba France), respectively. An X-ray photoelectron spectroscopy (XPS, ESCALAB 250, USA) was used to investigate the elemental valence and content of the alloy surface.

2.4. Electrochemical measurements

The electrochemical measurements were carried out by an H-type electrolytic cell configured with a Celgard 3501 membrane using an electrochemical workstation (DH 7001, Donghua), the Ar-saturated 30 mL of 0.5 M Na_2SO_4 + 0.1 M KNO_3 solution was in each chamber of the H-type electrolytic cell. The copper−cobalt alloy loaded on CFP (1.0 × 0.5 cm^2) was used as the working electrode, while Pt-plate and saturated calomel electrode (SCE) were the counter and reference electrodes, respectively. The linear sweep voltammetry (LSV) tests were performed with the scan rate of 5 mV/s. The potential difference between RHE and saturated calomel electrode was measured to be 0.95 V in 0.5 M Na_2SO_4 solution, and the reference potentials involved in this work have been uniformly transformed into the RHE. The ammonia yield and Faraday efficiency of copper−cobalt alloy were studied by the chronoamperometry (CA) tests for 30 min. The current density is obtained according to the geometric area (1.0 × 0.5 cm^2) of the electrode since the carbon fiber paper is double-sided. The electrochemical impedance spectroscopy (EIS) was carried out to study the kinetics of the electrode process at −0.05 V vs. RHE from 0.1 kHz to 100 kHz by an electrochemical work station [21].

2.5. Determination of products

The NH_3 concentration of electrolyte performed by CA was detected by UV−vis spectrophotometer (TU-1810, Puxi, Beijing), as follows.

Determination of NH_3: The NH_3 concentration was determined by the indophenol blue methods. Firstly, 0.5 g of NaOH and 1 mL of NaClO were dissolved and mixed in 100 mL of deionized water to obtain the coloring agent “A”. 5 g of sodium salicylate, 0.02 g of sodium nitroprusside and 0.25 g of NaOH were dissolved in 50 mL of deionized water to get the coloring agent “B”. Then, the diluted electrolyte performed by 30 min CA (2 mL) was mixed with the coloring agents A (0.5 mL) and B (0.5 mL), and let stand for 1 h. The concentration of NH_3 was calculated from the calibration curve (Fig. S2) by analyzing the absorption intensity at the wavelength of ~660 nm. The calibration curve was plotted with different known concentrations of ammonia and their corresponding absorption intensity.

Isotope Labeling Experiments: The 0.1 M $K^{15}NO_3$ (99%) and 0.5 M Na_2SO_4 mixed solution was used as the electrolyte to implement the CA tests. 900 μL of the reacted solution was mixed with 1 M H_2SO_4 (25 μL), deuterium dimethyl sulfoxide (DMSO-D6, 50 μL) and maleic acid ($C_4H_4O_4$, 0.0046 g) for further ^1H NMR detection. The concentration of generated $^{15}NH_3$ was further quantified by fitting the standard curve of the integrated area by employing $C_4H_4O_4$ as an external standard. After adding the H_2SO_4, DMSO-D_6 and $C_4H_4O_4$, the solutions of $^{15}NH_3$ with known concentrations (500, 1000, 2000, 4000 and 6000 μmol/L) were detected by ^1H NMR (AVANCE III HD 600 M HZ) to obtain a series of integrated areas to build the standard curve (Fig. S5).

2.6. Calculation of the electrochemical performance

The Faradaic efficiency (FE) and ammonia yield were calculated as follows [22,23]:

$$FE = (8F \times c_{NH3} \times V) / Q \quad (1)$$

Where F is the Faradaic constant (96485 C/mol), c_{NH3} is the molar concentration of generated NH_3, V is the electrolyte volume (30 mL) in the cathode chamber, and Q is the total charge passing the electrode.

$$Yield\ (NH_3) = (c_{NH3} \times V) / (t \times S) \quad (2)$$

Where t is the reaction time (30 min), and S is the geometric area of the working electrode (0.5 cm^2).

2.7. Computational details

The first-principle DFT calculations were performed by Vienna Ab initio Simulation Package (VASP) with the projector augmented wave (PAW) method. The exchange functional was treated using the generalized gradient approximation (GGA) of Perdew Burke-Ernzerhof (PBE) functional [24]. Copper-cobalt alloys were constructed by replacing Cu atoms with Co atoms based on the Cu (111) surface. Five models with four-layer 3 × 3 supercell were constructed for the simulation calculations of Cu, Cu_5Co, $Cu_{2.5}Co$, CuCo and Co (Fig. S8). The energy cutoff for the plane wave basis expansion was set to 500 eV, and the force on each atom less than 0.03 eV/Å was set for the convergence criterion of geometry relaxation. The Brillouin-zone integration was sampled by a Γ-centered 4 × 4 × 1 Monkhorst–Pack k-point. The self-consistent calculations applied a convergence energy threshold of 10^{-6} eV. The DFT-D3 method was employed to consider van der Waals interactions. Since the NRA proceeded in an aqueous environment and the NRA involved *H transfer, solvation effects were considered by VASPsol. Dipole corrections were included in all computations to minimize inaccuracies in the total energy because of simulated slab interactions. The adsorption free energy was calculated as follows: $\Delta G_{ads} = \Delta E_{total} + \Delta ZPE - T\Delta S + \Delta G_U + \Delta G_{pH}$, where ΔE is the reaction energy obtained by the total energy difference between the reactant and product molecules absorbed on the catalyst surface, ΔZPE is the correction of zero-point energy, T is the temperature (K), and ΔS is the entropy change, ΔG_U is the free energy contribution connected to electrode potential U [25]. The free energies of reactions that H^+ takes part in are corrected as follows: $\Delta G_H = -k_BT \times pH \times \ln 10$, where k_B is Boltzmann's constant and T is the temperature [26].

3. Result and discussion

The SEM images of CFP (Fig. 1a), Cu-CFP (Fig. 1b), Cu_5Co-CFP (Fig. 1c), $Cu_{2.5}Co$-CFP (Fig. 1d), CuCo-CFP (Fig. 1e) and Co-CFP (Fig. 1f) demonstrate the interwoven 4 μm-diameter carbon fibers and highly dispersed metal particles, the rough grooved structure of the CFP surface facilitates the adhesion of the precursor and the anchoring of metal atoms during the carbothermal shock process. The bound water and chlorine (Cl) atoms in the precursor can react with hydrogen and carbon atoms on the CFP surface in the very short high-temperature process. The generated impact gases during this process promote the generation of small metal particles and their dispersion uniformity [19]. The TEM image of $Cu_{2.5}Co$-CFP is shown in Fig. 1g, the high-resolution TEM (HR-TEM, Fig. 1h) of it displays the lattice fringes with the interplanar spacings of 0.207 nm, which can be assigned to the (111) planes of $Cu_{2.5}Co$ alloy, the inset of Fig. 1h shows a uniform distribution of alloy atoms. The HAADF and elemental mapping (Fig. 1i–k) demonstrate the compositional uniformity of $Cu_{2.5}Co$-CFP.

The XRD patterns of pure CFP, Cu-CFP, Cu_5Co-CFP, $Cu_{2.5}Co$-CFP, CuCo-CFP and Co-CFP are shown in Fig. 2a, the diffraction peaks of 26.5° and 54.5° are associated with the graphitic carbon structure, which can be assigned to the (002) and (004) plane, respectively. The diffraction peaks at 43.3°, 50.5°, 44.2° and 51.5° are corresponding to Cu(111), Cu(200) of the face-centered cubic (FCC) Cu

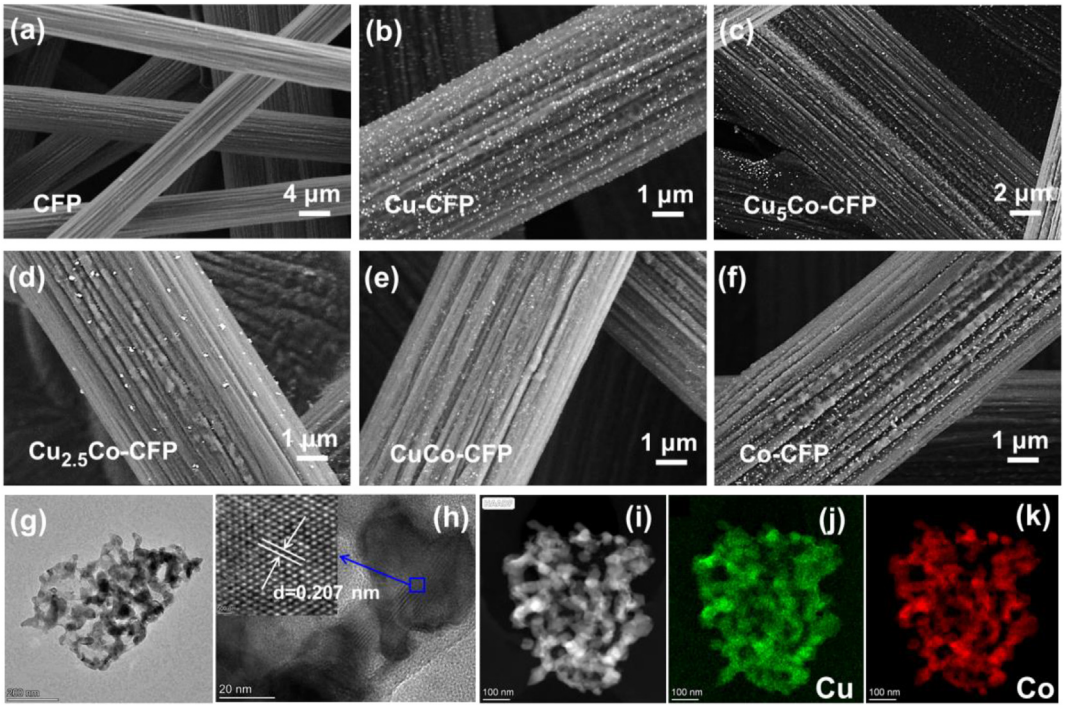

Fig. 1. The SEM images of CFP (a), Cu-CFP (b), Cu_5Co-CFP (c), $Cu_{2.5}Co$-CFP (d), CuCo-CFP (e), and Co-CFP (f). The TEM (g), HR-TEM images (h), HAADF image (i), and elemental mapping (j–k) of $Cu_{2.5}Co$-CFP.

(JCPDS 04−0836) and Co(111), Co(200) of FCC Co (JCPDS 15−0806), respectively. The Cu-CFP and Co-CFP exhibit weak diffraction peaks at the above angles indicating that the Co and Cu prepared by the carbothermal shock are FCC metals with ultra-small crystal regions, further demonstrating the feasibility of the method in the synthesis of highly dispersed FCC copper-nickel alloys [27,28]. The Raman spectra of pure CFP, Cu-CFP, Cu_5Co-CFP, $Cu_{2.5}Co$-CFP, CuCo-CFP and Co-CFP are demonstrated in Fig. 2b, three obvious peaks at 1348, 1595 and 2692 cm^{-1} can be assigned to the D, G and 2D band of graphitic carbon [29], the D/G ratios obtained on them are in the 0.05−0.1 range. Otherwise, no other peaks are observed in the whole region, which can be associated with the absence of optical phonons in metal.

The XPS was performed to study the surface chemical valence information of copper−cobalt alloys on CFP (Fig. S1). The high-resolution XPS (HR-XPS) of the Cu2p core-level region of the copper−cobalt alloys are shown in Fig. 2c, which can be deconvoluted to XPS signals of Cu (0) ($2p_{3/2}$, 932.9 eV) and Cu (II) ($2p_{3/2}$, 934.5 eV) species which reveals the presence of CuO in the surface of copper−cobalt alloys. The HR-XPS of Co2p core-level regions of the copper−cobalt alloys are shown in Fig. 2d, which can be deconvoluted to XPS signals of Co (II) ($2p_{3/2}$, 779.9 eV) species which indicates that the cobalt element on the surface is mainly in the form of CoO on the surface of copper−cobalt alloys [30]. The surface oxidation state detected by XPS with very high sensitivity can be attributed to the oxidation of the highly active catalyst in the air. Traces of oxidized Cu and Co on the surface can be easily reduced to the metallic state at negative potentials to facilitate enhanced catalytic activity for nitrate.

The electrocatalytic NRA activity of the copper−cobalt alloys was investigated in 0.5 M Na_2SO_4 solution with 0.1 M KNO_3 by an H-cell assembled with a Celgard 3501 membrane. Fig. 3a shows the IR-corrected LSV curves of copper−cobalt alloys load on CFP, the $Cu_{2.5}Co$-CFP alloy has a good overlap with the LSV curve of Cu-CFP with outstanding NRA activity at low overpotential region (+0.05 ~ +0.3 V vs. RHE), and the $Cu_{2.5}Co$-CFP alloy has the highest current density in the high overpotential region (−0.2 ~ +0.05 V vs. RHE). The Co-CFP has the lowest onset potential except for pure CFP, and no declining inflection point of the LSV is observed throughout the whole range (−0.3 ~ +0.3 V vs. RHE), which is mainly attributed to the poor NRA activity of cobalt. As shown in Fig. 3a, the declining inflection point of the LSV curve of $Cu_{2.5}Co$-CFP at −0.15 V vs. RHE can be attributed to the repulsion of NO_3^- by the negatively charged electrode surface and the attraction of H^+ at a negative potential, it can also be used to explain the declining inflection points of LSV curves generated by other samples at high overpotentials.

Fig. 3b provides the Tafel plots to demonstrate the reaction kinetics of copper−cobalt alloys which are obtained by replotting the corresponding LSV curves according to the previously reported formula [31]. The Tafel slope is inversely proportional to the charge transfer coefficient, the $Cu_{2.5}Co$-CFP alloy has a small Tafel slope value of 108 mV/dec, and the addition of certain Co can reduce the Tafel slope of the Cu-CFP and enhance the reaction rate of rate-determining step, owing to the fact that the high d-band center of Co raises the d-band center of Cu. In addition, the surface Co with strong adsorption energy can provide abundant highly reactive H free radical, which is favorable for reducing the intermediate products in the NRA process. The EIS spectra and the of copper−cobalt alloys are shown in Fig. 3c, the $Cu_{2.5}Co$-CFP alloy has the smallest diameter of the semicircle with the charge transfer resistance of 4.5 Ω and the fastest kinetics for NRA, which is consistent with the results of the Tafel slope.

As shown in Fig. 3d, the LSV curve of $Cu_{2.5}Co$-CFP in blank solution (without NO_3^- and NO_2^-) is almost the same as that of CFP,

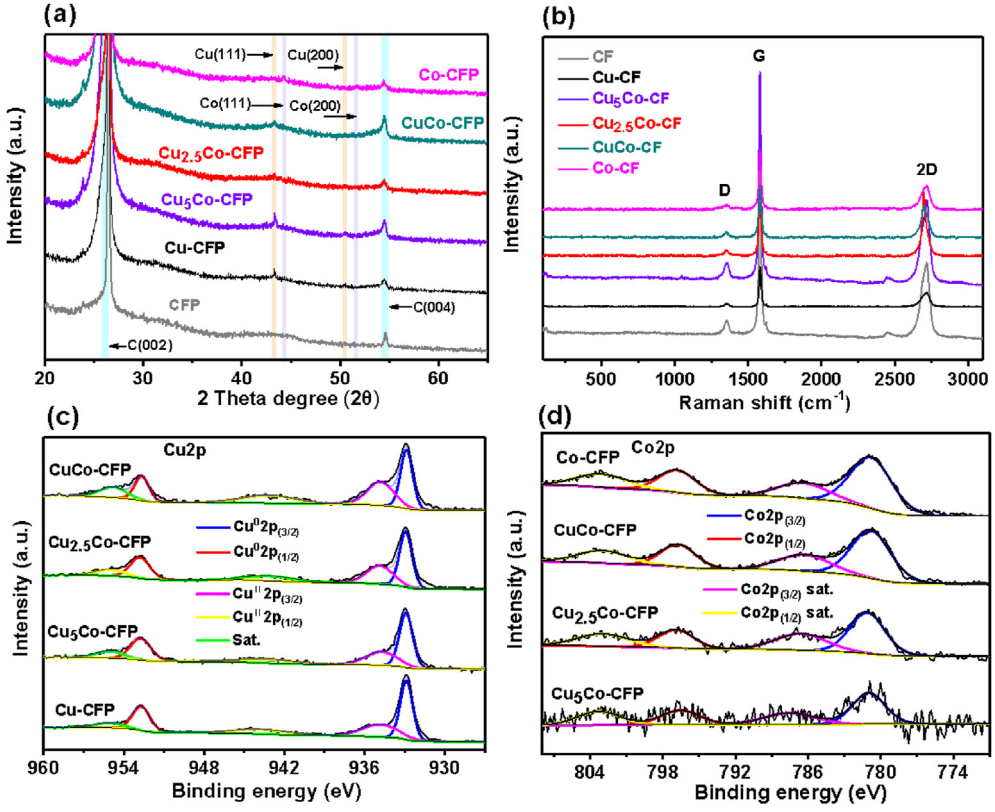

Fig. 2. The XRD patterns (a), Raman spectra (b), Cu2p HR-XPS (c), and Co2p (d) HR-XPS spectra of CFP, Cu-CFP, Cu_5Co-CFP, $Cu_{2.5}Co$-CFP, CuCo-CFP, and Co-CFP.

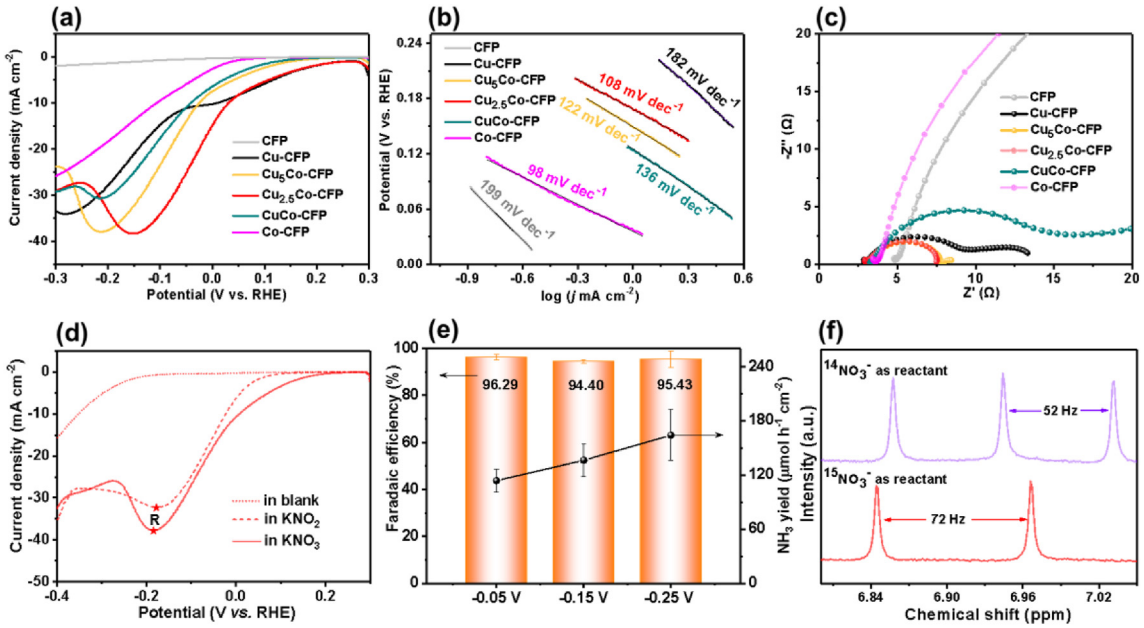

Fig. 3. (a) LSV curves, (b) Tafel slopes, and (c) EIS spectra of CFP, Cu-CFP, Cu_5Co-CFP, $Cu_{2.5}Co$-CFP, CuCo-CFP, and Co-CFP in 0.1 M KNO_3, (d) LSV curves of $Cu_{2.5}Co$-CFP in blank, 0.1 M KNO_3 and 0.1 M KNO_2 solutions, (e) Faradaic efficiency and NH_3 yield of $Cu_{2.5}Co$-CFP at different potentials, (f) ^1H NMR spectra of electrolyte performed by $Cu_{2.5}Co$-CFP using $^{14}NO_3^-$ and $^{15}NO_3^-$ as N-source.

indicating the current density is mainly contributed by the NRA activity of the material itself. The LSV curve of $Cu_{2.5}Co$-CFP alloy in 0.1 M nitrite (NO_2^-) and nitrate (NO_3^-) solution exhibits a reduction peak near −0.18 V, respectively. Interestingly, the current density of the $Cu_{2.5}Co$-CFP alloy in NO_2^- solution is greater than that in NO_3^- solution in the range of 0 ~ + 0.2 V vs. RHE. It is evident that the cathodic current in the region of 0 ~ +0.2 V vs. RHE mainly originates from the reduction of NO_3^- to NO_2^-. The slope of the LSV curve in the range of 0 ~ + 0.2 V vs. RHE is smaller than that in the range of −0.2 ~ 0 V vs. RHE, indicating the slow reaction kinetics of NO_3^- to NO_2^-.

The NH_3 yield and Faradaic efficiency of the $Cu_{2.5}Co$-CFP alloy were studied by the CA at −0.05, −0.15, −0.25 V vs. RHE within 30 min in Ar-saturated 0.1 M KNO_3 solution with 0.5 M Na_2SO_4. The CA curves at different potentials are presented in Fig. S3a, and the corresponding UV−vis absorption spectra of the electrolytes by the indophenol blue method are shown in Fig. S3b. The $Cu_{2.5}Co$-CFP alloy achieves the maximum NH_3 yield of 164.23 μmol/h/cm^2 at −0.25 V vs. RHE and the maximum Faradaic efficiency of 96.29% at −0.05 V vs. RHE. Within a certain range, a high overpotential favors the reaction rate, while a low overpotential helps to enhance the reaction selectivity, which is consistent with the previously reported articles [7,32,33]. Subsequently, the $Cu_{2.5}Co$-CFP alloy was carried out in a blank control experiment with an electrolyte containing only Na_2SO_4, the corresponding CA curves, UV−vis absorption spectra, and NH_3 yield are shown in Figs. S4a−4c, almost no NH_3 was found in the electrolyte, proving that the reaction current comes mainly from the conversion of NO_3^-.

To further verify the reliability of NRA reactivity of $Cu_{2.5}Co$-CFP alloy, $K^{15}NO_3$ was used as the original NO_3^- to perform the ^{15}N isotope labeling experiments. The ^1H NMR spectra (Fig. 3f) exhibit the obvious double peaks at 6.84 and 6.96 ppm with a coupling constant of 72 Hz [34−36], indicating that the reaction product only contains the $^{15}NH_4^+$. According to the ^1H NMR results, the NH_3 generation rate of $Cu_{2.5}Co$-CFP alloy was determined to be 157.06 μmol/h/cm^2, which is in general agreement with the data (164.23 μmol/h/cm^2) obtained from the UV−vis determination, and finally confirming the reliability of the reaction on $Cu_{2.5}Co$-CFP alloy. The cycling stability of $Cu_{2.5}Co$-CFP alloy is shown in Fig. S6a, which maintains a significant NH_3 yield of 129.35 μmol/h/cm^2 with the Faradaic efficiency of 89.52% after 6 cycles. The corresponding CA curves and UV−vis absorption spectra of it at different cycles are shown in Fig. S7. The SEM images and full-scan XPS spectra of $Cu_{2.5}Co$-CFP alloy after the durability test are shown in Figs. S6b−S6d, the morphological structure and elemental content of the alloy are still maintained, indicating the stability of $Cu_{2.5}Co$-CFP alloy during the continuous long reaction time. The two additional peaks that appeared after the durability test are the Na 1s peak and the Na auger peak, which can be attributed to the adsorption of sodium ions in the electrolyte [37].

The reaction free energies for NO_3^- adsorption (pH = 7, Fig. 4a) on Cu (111), Cu_5Co (111), $Cu_{2.5}Co$ (111), Cu_1Co (111), and Co (111) are the thermodynamically up-hill processes with the free energy changes (ΔG) of 0.13, 0.28, 0.29, 0.43, and 0.53 eV, respectively. The ΔG for NH_3 desorption on them are 0.36, 0.33, 0.32, 0.20, and −0.16 eV, respectively. The ΔG for the *NO → *N step on them are −0.05, 0.20, 0.24, 0.14, and −0.16 eV, respectively. Therefore, $Cu_{2.5}Co$ has the lowest reaction energy barrier in the whole NRA reaction process with the potential-determining step (PDS, 0.32 eV) of NH_3 desorption. For electron transfer processes, at low overpotentials (e.g., 0 eV), Cu has a faster reaction rate due to a lower energy barrier, whereas at high overpotential (e.g., −0.25 eV), $Cu_{2.5}Co$ overcomes the energy barrier of *NO → *N step and exhibits a higher reaction rate due to a smaller energy barrier for ammonia desorption, which is consistent with the experimental results. The calculated Cu-3d partial density of states (PDOS) (Fig. 4b) indicates that the increase of Co content can elevate the d-band center of Cu. The projected crystal orbital Hamilton population (pCOHP) calculations (Fig. 4c) were performed for Cu−N on Cu (111) and $Cu_{2.5}Co$ (111) with adsorbed NH_3, the addition of Co makes some of the electrons go into the antibonding orbitals of Cu−N, which promotes the desorption of NH_3.

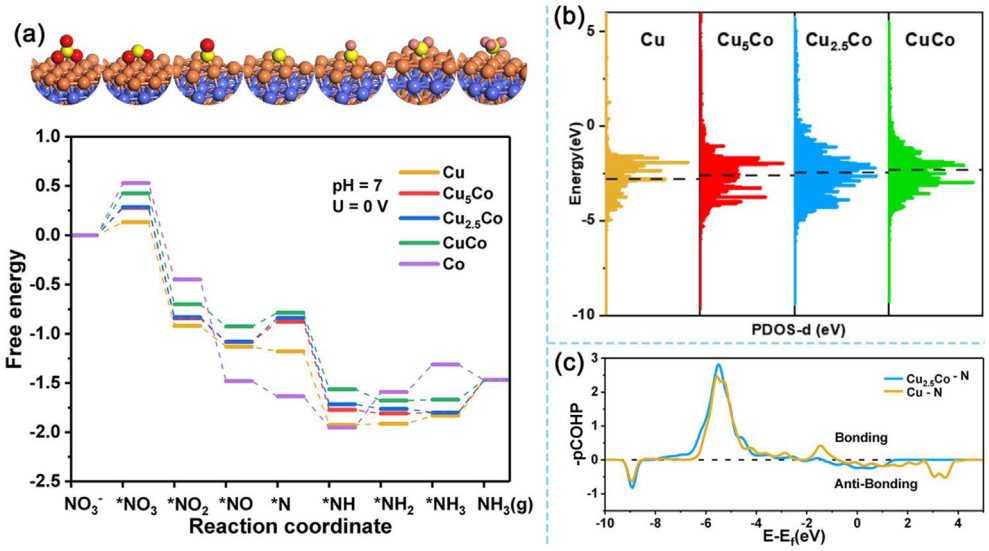

Fig. 4. (a) The free energy diagrams of NRA (pH = 7, U = 0 V) via the N-end pathway on Cu, Cu_5Co, $Cu_{2.5}Co$, CuCo, and Co surface, respectively. (b) The Cu-3d PDOS of Cu, Cu_5Co, $Cu_{2.5}Co$, and Cu_1Co. (c) The pCOHP of Cu—N bond for Cu and $Cu_{2.5}Co$ surface with adsorbed NH_3.

4. Conclusions

In summary, a highly dispersed FCC $Cu_{2.5}Co$ alloy was successfully developed by ultrafast carbothermal shock for high-activity NRA catalyst. The potential-dependent NRA activity of $Cu_{2.5}Co$ alloy was verified from experiments and theoretical calculations. The addition of Co atoms enhances the NRA activity of monometallic Cu in the high overpotential region, while it has little effect in the low potential region. The NRA activity increases most when the ratio of Cu to Co is 2.5, achieving the highest ammonia yield of 164.23 μmol/h/cm^2 and Faradaic efficiency of 96.29% at −0.25 V and −0.05 V vs. RHE. This work provides a new strategy of material preparation for the alloying mechanism to enhance the NRA activity of monometallic Cu and provides an experimental reference for the reaction kinetics study.

CRediT author statement

Chen Ye: Software, Methodology, Software, Writing - original draft preparation. **Zhao Yaling**: Data curation, Validation. **Zhao Ziwei**: Visualization, Investigation, Formal analysis. **Liu Yang:** Conceptualization, Writing - reviewing and editing, Supervision.

Declaration of competing interest

The authors declare that they have no known competing financial interests or personal relationships that could have appeared to influence the work reported in this paper.

Data availability

Data will be made available on request.

Acknowledgments

This work was supported by the Special Project of Henan Provincial Key Research, Development and Promotion (Science and Technology) (Grant No. 212102310060, 222102320147), the Fellowship of China Postdoctoral Science Foundation (Grant No. 2021M701116, 2021M690930), the Key Scientific Research Project of Henan Province Higher Education of China (Grant No. 21A430020), the Scientific and Technological Research Project of Xinxiang, China (Grant No. GG2020020) and LvLiang Cloud Computing Center of China (TianHe-2).

Appendix A. Supplementary data

Supplementary data to this article can be found online at https://doi.org/10.1016/j.mtener.2022.101112.

References

[1] G.F. Chen, Y. Yuan, H. Jiang, S.Y. Ren, L.X. Ding, L. Ma, T. Wu, J. Lu, H. Wang, Electrochemical reduction of nitrate to ammonia via direct eight-electron transfer using a copper–molecular solid catalyst, Nat. Energy 5 (2020) 605–613, https://doi.org/10.1038/s41560-020-0654-1.
[2] G.A. Cerrón-Calle, A.S. Fajardo, C.M. Sánchez-Sánchez, S. Garcia-Segura, Highly reactive Cu-Pt bimetallic 3D-electrocatalyst for selective nitrate reduction to ammonia, Appl. Catal. B Environ. 302 (2022) 120844, https://doi.org/10.1016/j.apcatb.2021.120844.
[3] P. Li, Z. Jin, Z. Fang, G. Yu, A single-site iron catalyst with preoccupied active centers that achieves selective ammonia electrosynthesis from nitrate, Energy Environ. Sci. 14 (2021) 3522–3531, https://doi.org/10.1039/d1ee00545f.
[4] Y. Liu, B. Huang, X. Chen, Z. Tian, X. Zhang, P. Tsiakaras, P.K. Shen, Electrocatalytic production of ammonia: biomimetic electrode–electrolyte design for efficient electrocatalytic nitrogen fixation under ambient conditions, Appl. Catal. B Environ. 271 (2020) 118919, doi: 10.1016/j.apcatb.20.
[5] Y. Liu, X. Zhang, Z. Chen, X. Zhang, P. Tsiakaras, P.K. Shen, Electrocatalytic reduction of nitrogen on FeAg/Si for ammonia synthesis: a simple strategy for continuous regulation of faradaic efficiency by controlling H^+ ions transfer rate, Appl. Catal. B Environ. 283 (2021) 119606, doi: 10.1016/j.apcatb.20.
[6] F. Lei, W. Xu, J. Yu, K. Li, J. Xie, P. Hao, G. Cui, B. Tang, Electrochemical synthesis of ammonia by nitrate reduction on indium incorporated in sulfur doped graphene, Chem. Eng. J. 426 (2021), 131317, https://doi.org/10.1016/j.cej.2021.131317.
[7] D. Hao, Y. Liu, S. Gao, H. Arandiyan, X. Bai, Q. Kong, W. Wei, P.K. Shen, B.J. Ni, Emerging artificial nitrogen cycle processes through novel electrochemical and photochemical synthesis, Mater. Today 46 (2021) 212–233, https://doi.org/10.1016/j.mattod.2021.01.029.
[8] T. Ren, K. Ren, M. Wang, M. Liu, Z. Wang, H. Wang, X. Li, L. Wang, Y. Xu, Concave-convex surface oxide layers over copper nanowires boost electrochemical nitrate-to-ammonia conversion, Chem. Eng. J. 426 (2021), 130759, https://doi.org/10.1016/j.cej.2021.130759.
[9] Y. Zhao, Q. Li, Q. Cui, S.-Q. Ni, Nitrogen recovery through fermentative dissimilatory nitrate reduction to ammonium (DNRA): carbon source comparison and metabolic pathway, Chem. Eng. J. 441 (2022), 135938, https://doi.org/10.1016/j.cej.2022.135938.
[10] S. Garcia-Segura, M. Lanzarini-Lopes, K. Hristovski, P. Westerhoff, Electrocatalytic reduction of nitrate: fundamentals to full-scale water treatment

applications, Appl. Catal. B Environ. 236 (2018) 546–568, https://doi.org/10.1016/j.apcatb.2018.05.041.
[11] X. Wang, M. Zhu, G. Zeng, X. Liu, C. Fang, C. Li, A three-dimensional Cu nanobelt cathode for highly efficient electrocatalytic nitrate reduction, Nanoscale 12 (2020) 9385–9391, https://doi.org/10.1039/c9nr10743f.
[12] X. Zhang, C. Wang, Y. Guo, B. Zhang, Y. Wang, Y. Yu, Cu clusters/TiO_{2-x} with abundant oxygen vacancies for enhanced electrocatalytic nitrate reduction to ammonia, J. Mater. Chem. A. 10 (2022) 6448–6453, https://doi.org/10.1039/D2.TA00661H.
[13] S.-E. Bae, A.A. Gewirth, Differential reactivity of Cu(111) and Cu(100) during nitratereduction in acid electrolyte, Faraday Discuss 140 (2009) 113–123, https://doi.org/10.1039/B803088J.
[14] S.-E. Bae, K.L. Stewart, A.A. Gewirth, Nitrate adsorption and reduction on Cu(100) in acidic solution, J. Am. Chem. Soc. 129 (2007) 10171–10180, https://doi.org/10.1021/ja071330n.
[15] Y. Zeng, C. Priest, G. Wang, G. Wu, Restoring the nitrogen cycle by electrochemical reduction of nitrate: progress and prospects, Small Methods 4 (2020), 2000672, https://doi.org/10.1002/smtd.202000672.
[16] Y. Wang, W. Zhou, R. Jia, Y. Yu, B. Zhang, Unveiling the activity origin of a copper-based electrocatalyst for selective nitrate reduction to ammonia, Angew. Chem. Int. Ed. 59 (2020) 5350–5354, https://doi.org/10.1002/anie.201915992.
[17] Y. Wang, A. Xu, Z. Wang, L. Huang, J. Li, F. Li, J. Wicks, M. Luo, D.H. Nam, C.S. Tan, Y. Ding, J. Wu, Y. Lum, C.T. Dinh, D. Sinton, G. Zheng, E.H. Sargent, Enhanced nitrate-to-ammonia activity on copper-nickel alloys via tuning of intermediate adsorption, J. Am. Chem. Soc. 142 (2020) 5702–5708, https://doi.org/10.1021/jacs.9b13347.
[18] J. Li, G. Zhan, J. Yang, F. Quan, C. Mao, Y. Liu, B. Wang, F. Lei, L. Li, A.W.M. Chan, L. Xu, Y. Shi, Y. Du, W. Hao, P.K. Wong, J. Wang, S.X. Dou, L. Zhang, J.C. Yu, Efficient ammonia electrosynthesis from nitrate on strained ruthenium nanoclusters, J. Am. Chem. Soc. 142 (2020) 7036–7046, https://doi.org/10.1021/jacs.0c00418.
[19] Y. Yao, Q. Dong, L. Hu, Overcoming immiscibility via a milliseconds-long "shock" synthesis toward alloyed nanoparticles, Matter 1 (2019) 1451–1453, https://doi.org/10.1016/j.matt.2019.11.006.
[20] Y. Yao, Z. Huang, P. Xie, S.D. Lacey, R.J. Jacob, H. Xie, F. Chen, A. Nie, T. Pu, M. Rehwoldt, D. Yu, M.R. Zachariah, C. Wang, R. Shahbazian-Yassar, J. Li, L. Hu, Carbothermal shock synthesis of high-entropy-alloy nanoparticles, Science 359 (2018) 1489–1494, https://doi.org/10.1126/SCIENCE.AAN5412.
[21] Z. Wang, S.D. Young, B.R. Goldsmith, N. Singh, Increasing electrocatalytic nitrate reduction activity by controlling adsorption through PtRu alloying, J. Catal. 395 (2021) 143–154, https://doi.org/10.1016/j.jcat.2020.12.031.
[22] J. Sun, W. Kong, Z. Jin, Y. Han, L. Ma, X. Ding, Y. Niu, Y. Xu, Recent advances of MXene as promising catalysts for electrochemical nitrogen reduction reaction, Chin. Chem. Lett. 31 (2020) 953–960, https://doi.org/10.1016/j.cclet.2020.01.035.
[23] N. Lazouski, M. Chung, K. Williams, M.L. Gala, K. Manthiram, Non-aqueous gas diffusion electrodes for rapid ammonia synthesis from nitrogen and water-splitting-derived hydrogen, Nat. Catal. 3 (2020) 463–469, https://doi.org/10.1038/s41929-020-0455-8.
[24] Q. Gao, H.S. Pillai, Y. Huang, S. Liu, Q. Mu, X. Han, Z. Yan, H. Zhou, Q. He, H. Xin, H. Zhu, Breaking adsorption-energy scaling limitations of electrocatalytic nitrate reduction on intermetallic CuPd nanocubes by machine-learned insights, Nat. Commun. 13 (2022) 2338, https://doi.org/10.1038/s41467-022-29926-w.
[25] B. Wang, Y. Yao, X. Yu, C. Wang, C. Wu, Z. Zou, Understanding the enhanced catalytic activity of high entropy alloys: from theory to experiment, J. Mater. Chem. A. 9 (2021) 19410–19438, https://doi.org/10.1039/d1ta02718b.
[26] J.X. Liu, D. Richards, N. Singh, B.R. Goldsmith, Activity and selectivity trends in electrocatalytic nitrate reduction on transition metals, ACS Catal. 9 (2019) 7052–7064, https://doi.org/10.1021/acscatal.9b02179.
[27] B. Liu, L. Zhang, W. Xiong, M. Ma, Cobalt-nanocrystal-assembled hollow nanoparticles for electrocatalytic hydrogen generation from neutral-pH water, Angew. Chem. 128 (2016) 6837–6841, https://doi.org/10.1002/ange.201601367.
[28] Y. Shi, Y. Wang, W. Yang, J. Qin, Q. Bai, Z. Zhang, Vapor phase dealloying-driven synthesis of bulk nanoporous cobalt with a face-centered cubic structure, CrystEngComm 23 (2021) 6526–6532, https://doi.org/10.1039/d1ce00883h.
[29] Y. Zhao, Y. Liu, Z. Zhang, Z. Mo, C. Wang, S. Gao, Flower-like open-structured polycrystalline copper with synergistic multi-crystal plane for efficient electrocatalytic reduction of nitrate to ammonia, Nano Energy 97 (2022), 107124, https://doi.org/10.1016/j.nanoen.2022.107124.
[30] Q. Liu, L. Xie, J. Liang, Y. Ren, Y. Wang, L. Zhang, L. Yue, T. Li, Y. Luo, N. Li, B. Tang, Y. Liu, S. Gao, A.A. Alshehri, I. Shakir, P.O. Agboola, Q. Kong, Q. Wang, D. Ma, X. Sun, Ambient ammonia synthesis via electrochemical reduction of nitrate enabled by $NiCo_2O_4$ nanowire array, Small 18 (2022), 2106961, https://doi.org/10.1002/smll.202106961.
[31] Y. Liu, S. Yin, P.K. Shen, Asymmetric 3d electronic structure for enhanced oxygen evolution catalysis, ACS Appl. Mater. Interfaces 10 (2018) 23131–23139, https://doi.org/10.1021/acsami.8b06106.
[32] H. Yin, Z. Chen, S. Xiong, J. Chen, C. Wang, R. Wang, Y. Kuwahara, J. Luo, H. Yamashita, Y. Peng, J. Li, Alloying effect-induced electron polarization drives nitrate electroreduction to ammonia, Chem Catal 1 (2021) 1088–1103, https://doi.org/10.1016/j.checat.2021.08.014.
[33] J. Yuan, Z. Xing, Y. Tang, C. Liu, Tuning the oxidation state of Cu electrodes for selective electrosynthesis of ammonia from nitrate, ACS Appl. Mater. Interfaces 13 (2021) 52469–52478, https://doi.org/10.1021/acsami.1c10946.
[34] Z. Deng, J. Liang, Q. Liu, C. Ma, L. Xie, L. Yue, Y. Ren, T. Li, Y. Luo, N. Li, B. Tang, A. Ali Alshehri, I. Shakir, P.O. Agboola, S. Yan, B. Zheng, J. Du, Q. Kong, X. Sun, High-efficiency ammonia electrosynthesis on self-supported Co_2AlO_4 nanoarray in neutral media by selective reduction of nitrate, Chem. Eng. J. 435 (2022), 135104, https://doi.org/10.1016/j.cej.2022.135104.
[35] Z. Wang, X. Zhang, Z. Dai, W. Tian, P. Wang, Y. Xu, X. Li, L. Wang, H. Wang, Electroreduction of nitrogen to ammonia over bimetallic mesoporous RuAu film, Mater. Today Energy 23 (2022), 100920, https://doi.org/10.1016/j.mtener.2021.100920.
[36] J. Li, F. Wei, C. Dong, Z. Wang, Z. Xiu, X. Han, Recent progress of inorganic metal-based catalysts in electrocatalytic synthesis of ammonia, Mater. Today Energy 21 (2021), 100766, https://doi.org/10.1016/j.mtener.2021.100766.
[37] S. Liu, S. Yin, S. Jiao, H. Zhang, Z. Wang, Y. Xu, X. Li, L. Wang, H. Wang, Au nanowire modified with tannic acid for enhanced electrochemical synthesis of ammonia, Mater. Today Energy 21 (2021), 100828, https://doi.org/10.1016/j.mtener.2021.100828.